UCLA
UCLA Electronic Theses and Dissertations

Title
A Magnetomechanical Thermal Energy Harvester With A Reversible Liquid Interface

Permalink
https://escholarship.org/uc/item/12r2m85g

Author
He, Hong

Publication Date
2012

Peer reviewed|Thesis/dissertation

UNIVERSITY OF CALIFORNIA

Los Angeles

A MAGNETOMECHANICAL THERMAL ENERGY HARVESTER WITH A

REVERSIBLE LIQUID INTERFACE

A thesis submitted in partial satisfaction of the

requirements for the degree Master of Science

in Mechanical Engineering

By

Hong He

2012

ABSTRACT OF THE THESIS

A Magnetomechanical Thermal Energy Harvester

With A Reversible Liquid Interface

by

Hong He

Master of Science in Mechanical Engineering

University of California, Los Angeles, 2012

Professor Y. Sungtaek Ju, Committee Chair

A device that has the potential to provide electrical power to wireless sensors is investigated in this thesis. The device uses a ferromagnetic material to exploit the temperature difference between a heat source and a heat sink to produce oscillating motions and temperature polarizations, which can then be converted into electrical energy by piezoelectric materials and pyroelectric materials, respectively. One advantage of the proposed device is that it can exploit the characteristics of both piezoelectric materials and pyroelectric materials to harvest waste heat energy; therefore, it is expected to have

potential high power output and conversion efficiency. Furthermore, the advantages of the reversible liquid interface can be exploited in this device to improve its performance.

The work presented in this thesis uses a coupled thermal and mechanical mathematical model to optimize the design of the proposed device. Three important parameters used in the mathematical model, the spring constant, the capillary force and the magnetic force, are calculated and then validated with experimental results to ensure that the modeling predictions match the actual behaviors of the device.

The mathematical model is then solved, and the modeling results are validated with experimental results to confirm that the model is able to correctly predict the behaviors of the device with reasonable levels of accuracy. The oscillation frequency is an important parameter for the device operation because a higher oscillation frequency means that more electrical energy can be collected in a given amount of time. Thus, the oscillation frequency is used as an index to evaluate the performance of the device. A parametric study is conducted for some design parameters, including the liquid volume of the reversible liquid interface, the total gap distance and the cold surface temperature, to attempt to increase the oscillation frequency. The mathematical model predicts that the device can achieve a relatively high oscillation frequency when the optimized design parameters are used.

A thermal energy harvester using a ferromagnetic material with a reversible liquid interface is then physically built. Experiments are performed to study the effect of the reversible liquid interface on the performance of the device, and the results indicate that the reversible liquid interface can effectively increase the oscillation frequency in the low

hot surface temperature region. Finally, when the optimized design parameters predicted by the mathematical model are applied, the device achieves a maximum oscillation frequency of 8.3Hz at a hot surface temperature of 41.8°C.

The thesis of Hong He is approved.

Chang-Jin Kim

Adrienne S. Lavine

Y. Sungtaek Ju, Committee Chair

University of California, Los Angeles

2012

TABLE OF CONTENTS

Acknowledgements

At first, I would like to thank my advisor, Professor Y. Sungtaek Ju, who gave me a lot of guidance in regard to research throughout my time at UCLA. This work takes a lot of time and patience from him. I would also like to thank my committee members, Professors Adrienne Lavine and Chang-Jin Kim, for their valuable comments and suggestions.

I would like to express my appreciation to former and current group members in UCLA Multiscale Thermosciences Laboratory: Katie Bulgrin, Gilhwan Cha, Stephen Sharratt, Tanye Tang, Yanbing Jia, Yujia Zhan, Cheng Peng, and Jinda Zhuang. I am especially grateful to Katie Bulgrin, who gave me a lot of guidance for this work.

I would like to thank all my friends at UCLA for their support and encouragement. I don't feel lonely because of you.

Last but not least, I would like to appreciate my family for their encouragement, support, patience, and unconditional love. They are always devoted to me without asking for any reward. I love you!

Chapter 1. Introduction

1.1 Thermal energy harvester

Wireless sensor networks (WSN) have a variety of applications in different areas, such as environmental, structural, medical and military monitoring, and have been the focus of a large amount of research in past decades [1-2]. Networks of wireless sensors are used to sense and transmit data at many points over a given area, often in remote areas in which maintenance is difficult. Because these sensors are shrinking in size and becoming integrated onto small areas due to more advanced microfabrication technologies, long-lasting power supplies are necessary for these sensors to operate autonomously. To achieve the objective of developing such power supplies, energy harvesting from the environment of the sensor is essential. Commonly used mechanisms for energy harvesting in wireless sensors involve the conversion of mechanical vibrations, radio frequency waves and temperature gradients into electrical energy [3].

Vibration-based energy harvesters are devices that convert the energy of mechanical vibrations into electrical energy. The widely used conversion mechanisms in vibration-based energy harvesters are electromagnetic, piezoelectric, and electrostatic. An electromagnetic transducer has a magnet and a coil, and their relative motion as a result of vibration induces an electric current in the coil according to Faraday's law. Some electromagnetic energy harvesters [4, 5] have been proposed and implemented.

Piezoelectric transducers use piezoelectric materials as springs, and the mechanical strain in the piezoelectric materials produces a voltage difference. A series of piezoelectric energy harvesters with different structures have been developed [6, 7]. Electrostatic transducers have two parallel plates that form a variable capacitor. An environmental vibration results in a change in the capacitance by changing the distance between or the overlapping area of the two plates. The capacitor can be either charge constrained, where the voltage changes as the capacitance changes, or voltage constrained, where the charge changes as the capacitance changes. Some prototypes of electrostatic energy harvesters have been developed [8, 9]. However, vibration-based energy harvesters are only suitable for environments in which lasting vibrations exist. The vibration sources are often unsteady, and thus, a storage system is necessary to provide a continuous power source.

In many urban environments, there is background RF radiation due to telecommunication antennas and other radiation-emitting devices [10]. These waves have electromagnetic energy, which can be converted into electrical energy to provide power for wireless sensors with specific types of circuits. The major challenge for RF power generation is the low power density of this type of radiation. Furthermore, the incident power density in the far field is inversely proportional to the square of the distance from the source [11]. Therefore, RF energy harvesters that are far from RF sources are not able collect sufficient energy to power wireless sensors.

Thermal energy is another potentially abundant energy source for wireless sensors. Thermal energy can be converted into electrical energy in different ways. Thermoelectric power generators convert thermal energy into electrical energy directly. They utilize the

2

Seebeck effect to generate electrical currents in the presence of temperature gradients. However, the power output and the efficiency of thermoelectric power generation are low [12]. Thermoelectric power generation requires a large temperature gradient and is not suitable for applications in environments in which the temperature gradients are small [13]. Pyroelectric generation is another mechanism, where pyroelectric materials are used to generate electrical energy when the temperature varies over time [14].

This thesis presents a magnetomechancal thermal energy harvesting device that uses a ferromagnetic material, which was first proposed in the literature [15]. It is a two-step device that first converts thermal energy into mechanical energy and then converts the mechanical energy into electrical energy using piezoelectric materials. The simulation results obtained from a numerical model predict that the device could have a potential high power density with a small temperature gradient using the thermal interface [16, 17]. In addition to piezoelectric materials, pyroelectric materials can also be exploited in this device to further improve its power output and conversion efficiency.

1.2 Reversible liquid interface

Thermal transport across a solid-solid interface is often limited by the surface roughness, which reduces the actual contact area and traps a layer of air in between the surfaces, thus increasing the thermal resistance of the solid-solid interface. A large loading pressure (~1MPa) is necessary to achieve a small thermal contact resistance (10^{-4}m^2·K/W), even for micromachined silicon surfaces with nanometer-scale roughness [18]. Carbon nanotubes have been exploited as thermal interface materials due to their

high thermal conductivities[19]. However, a high loading pressure (0.445MPa) is still necessary to obtain a small thermal contact resistance (19.8mm^{2}K/W) because only a small fraction of the carbon nanotubes are in contact with the opposing surface. Furthermore, the thermal interface is not reversible due to the strong adhesion between the carbon nanotubes and the opposing surface [20].

A liquid interface can provide a small thermal contact resistance (5×10^{-5}m^{2}K/W) with a low loading pressure (1kPa) [21] because liquid is capable of making complete contact with solid surfaces and thus prevents a layer of air from being trapped between the solid surfaces. A liquid interface is also capable of overcoming some of the disadvantages of direct solid-solid contact interfaces, such as fracture, cold welding, and other failure mechanisms. Moreover, surface tension dominates over gravity at the microscale, and thus, the morphologies of the parallel columns of a dielectric liquid confined in microchannels can be reversibly changed, resulting in rapid and reliable thermal switching. However, the rupture distances of liquid bridges are often of similar magnitude to the lengths of the microchannels, which are typically ~1 mm, thus limiting the use of liquid interfaces in applications where limited actuation ranges or rapid thermal cycling are required. An alternative design that replaces microchannels with discrete circles to reduce the rupture distance has been reported [22]. This new design reduced the liquid volume for each discrete droplet, which determines the rupture distances of the liquid bridges.

A reversible liquid interface has potential applications in some thermal energy-related devices, including micro-bolometers, pulsed thermoelectric cooling devices,

solid-state electrocaloric refrigerators, pyroelectric waste heat harvesters, and satellite thermal management devices. Cha et al. demonstrated a pyroelectric energy harvester that incorporates a reversible liquid interface [23]. The material-level power densities of the device are on the order of 100 mW/cm^3 when thermodynamic cycle frequencies are on the order of 1 Hz. Jia et al. reported a solid-state refrigerator based on the electrocaloric effect [24] in which a reversible liquid interface was used to achieve reliable high-contrast thermal switching between an electrocaloric material and a heat source/sink.

This thesis will exploit the reversible liquid interface to improve the thermal energy transfer in a thermal energy harvester using a ferromagnetic material.

1.3 Principle of the device

Figure 1.1 shows a schematic of the thermal energy harvester with a reversible liquid interface. The thermal energy harvester is composed of a heat sink, a spring frame with a gadolinium plate placed in its center, a reversible liquid interface, a permanent magnet, and a heat source.

Gadolinium is a ferromagnetic material, and it has the special characteristic that its magnetization is temperature dependent: its magnetization increases when the temperature decreases and decreases when the temperature increases. As the gadolinium plate comes into contact with the surface of the heat sink, it cools. The magnetization of the gadolinium plate thus increases, and the magnetic force between it and the permanent magnet also increases. When the magnetic force exceeds the spring force exerted by the spring arm, the gadolinium plate begins to move toward the heat source, eventually

touching the liquid droplet and pressing down on to form a liquid film. The gadolinium is

heated, and the magnetic force decreases. Once the spring force is greater than the sum of

the magnetic force and the capillary force exerted by the liquid interface, the gadolinium

plate moves away from the heat source. The liquid bridge then ruptures, and the liquid

droplet recovers its original morphology due to surface tension. This process is repeated,

and the gadolinium plate oscillates between the heat sink and the heat source. The

oscillating motion of the gadolinium plate not only creates strains in the spring arm but

also produces temperature polarizations. If the spring arm is coated with piezoelectric

materials or is composed of piezoelectric materials, the strains in the spring arm will

produce a voltage output. Similarly, if the gadolinium plate is coated with pyroelectric

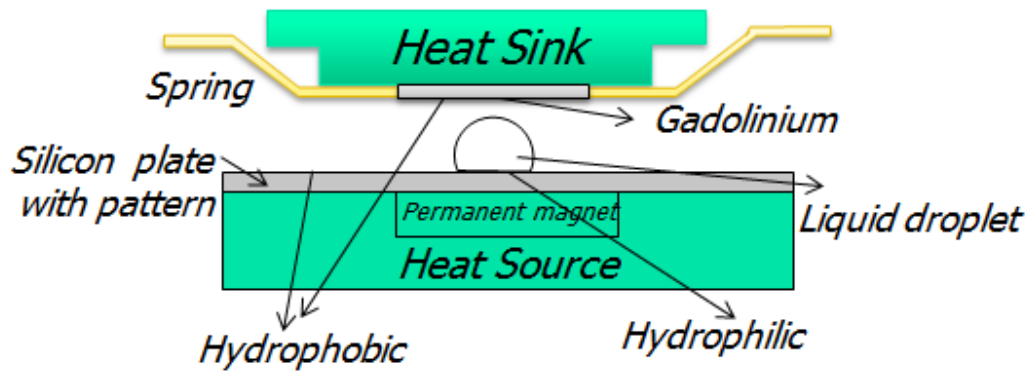materials, the temperature polarizations will induce a voltage output.

Figure 1.1 Schematic diagram of the thermal energy harvester with a reversible
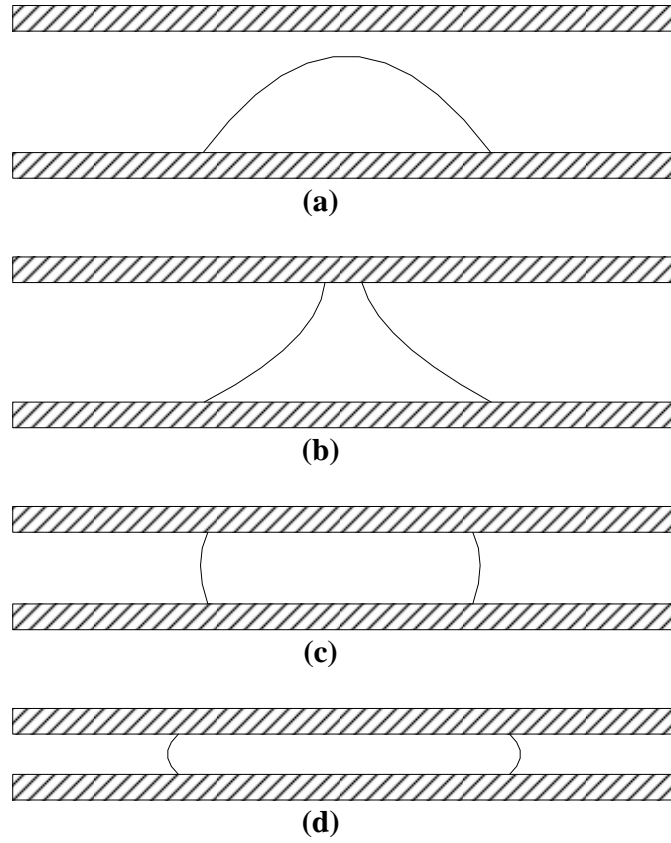
liquid interface

Figure 1.2 The morphological transitions of a liquid interface when the gadolinium plate approaches the substrate: (a) a liquid droplet is confined in the hydrophilic area; (b) a liquid bridge forms and has a negative mean curvature; (c) the liquid bridge has a positive mean curvature, but the droplet is still confined within the hydrophilic region; (d) the droplet spreads out of the hydrophilic region

Figure 1.2 presents the morphology of a liquid interface as it changes when the gadolinium plate moves toward the substrate. The droplet is initially confined in the hydrophilic area to minimize its surface energy (figure 1.2a). When the gadolinium plate makes contact with the liquid droplet, a liquid bridge with a negative mean curvature is

formed (figure 1.2b). As the gadolinium plate continues to approach the substrate, the contact angle increases until it reaches the advancing contact angle. The mean curvature of the liquid bridge gradually becomes positive, but the contact line is still pinned at the edges of the pattern (figure 1.2c). If the gadolinium plate continues to approach the substrate, the liquid droplet is pressed out of the pattern to form a thin liquid film (figure 1.2d). Finally, if the gadolinium plate moves away from the substrate, the liquid film recovers its original morphology due to surface tension.

Chapter 2. Calculations and experimental validations of the model parameters

2.1 Introduction

In this chapter, several important parameters in the coupled thermal and mechanical numerical model are calculated and then validated by experimental results. These parameters include the spring constant of the spring frame, the capillary force produced by the reversible liquid interface, and the magnetic force.

2.2 Spring constant of the spring frame

A mathematical model is set up with the finite-element analysis software COMSOL Multiphysics to calculate the spring constant of the spring frame, as illustrated in figure 2.1. The outer frame of the spring frame is attached to the stage. The inner square of the spring frame is the actuation plate, and it can move up and down. The gadolinium plate is placed in the central blank region of the actuation plate. The slim bar connecting the outer frame and the actuation plate is the spring arm, and deformation of the spring arm induces a spring force. A force is applied to the actuation plate, and the displacement of the actuation plate is predicted by the software. The spring constant is then calculated by Hooke's law

$$k = \frac{F}{x} \tag{2.1}$$

where F is the applied force and x is the corresponding displacement.

The spring frames fabricated for the thermal energy harvester are composed of an alloy of BeCu. The material properties are chosen from the material library of the simulation software. The dimension of the spring frame (frame 1 in the experiments) was measured with a caliper, which has a precision of ±0.01 mm. The simulation result is presented in figure 2.4 and is in agreement with the experimental result. The spring constant found by the simulation is 201.0N/m, while the experimental result is 205.7N/m.
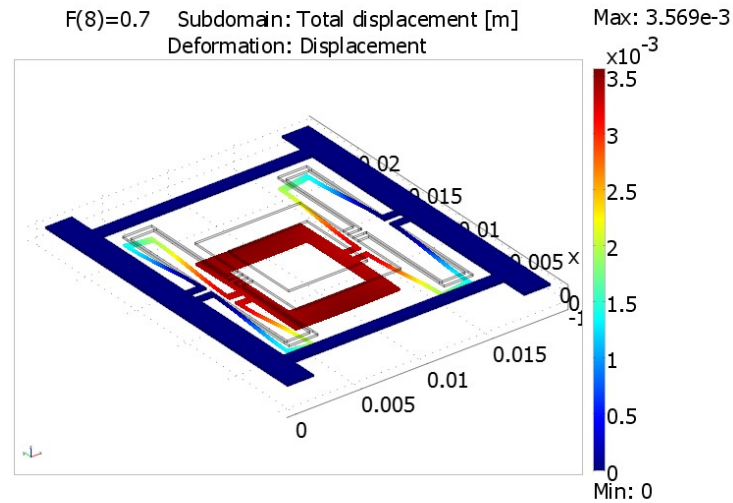
Figure 2.1 The model used to calculate the spring constant of the spring frame: the spring arm is deformed when force is applied to the actuation plate (the central square)
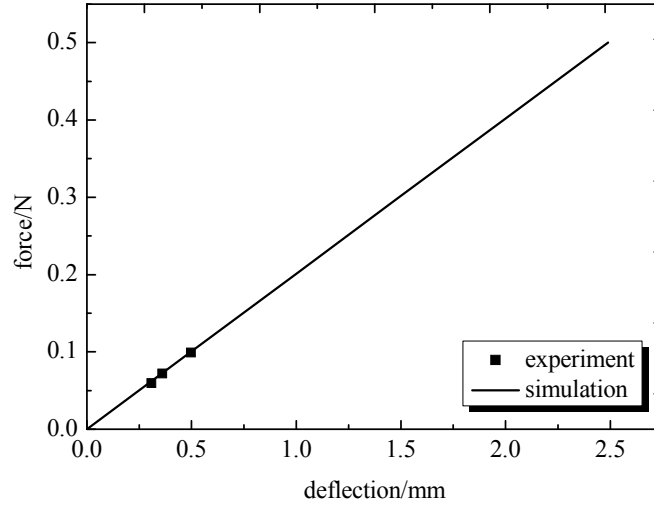
Figure 2.2 Spring constants found in the simulation and the experiment: the simulation result is 205.7N/m, and the experimental result is 201.0N/m

Figure 2.3 shows the experimental setup used to measure the spring constants of the spring frames. The spring frames are attached to a cantilever. Then, the spring arms are deformed by hanging weights on the actuation plates, and the deformations are optically recorded using a camera. Because the deflections are calculated using images recorded by the camera, there is an uncertainty in the deflection measurement of ±0.016 mm due to the two boundary pixels in the images. Two spring frames that were fabricated in the same batch as the one used in the thermal energy harvester are measured. The spring constant of frame 1 is 205.7N/m and that of frame 2 is 198.4N/m, as is illustrated in figure 2.4. Therefore, the design spring constant of the spring frame used in the thermal energy harvester is 200N/m, and the actual value is within ±2.85% of the design value.

11

Figure 2.3 Experimental setup for the measurement of the spring constants: the spring frames are deformed by weights, and the deformations are recorded optically
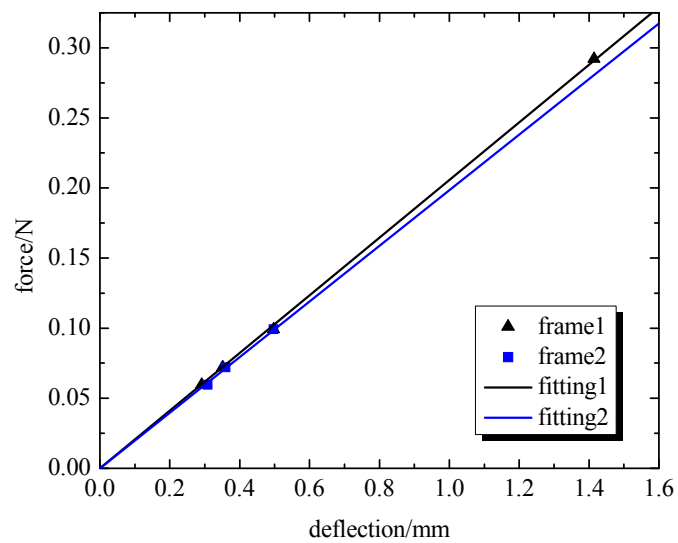
Figure 2.4 Spring constants of two spring frames: the spring constant of frame1 is 205.7N/m, the spring constant of frame2 is 198.4N/m, and the average value is 202.1N/m

2.3 Capillary force produced by the reversible liquid interface

The surface morphology transitions of the liquid interface include two periods: the droplet state and the film state. In the droplet state, the liquid droplet is confined within the hydrophilic area. The capillary force produced by the liquid interface in this state is calculated using the Surface Evolver model. In the film state, the liquid droplet is pressed out of the pattern and forms a layer of liquid film. The capillary force in this state is calculated using an analytical model, as shown schematically in figure 2.5.
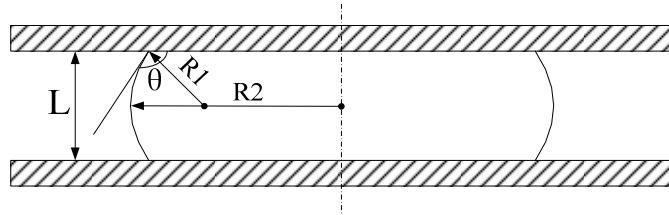

Figure 2.5 Schematic diagram of the analytical model to calculate the capillary force in the film state

The total force produced by the liquid interface comprises the Laplace pressure and the surface tension. According to the Young-Laplace equation, the Laplace pressure can be calculated as

$$P = \sigma\left(\frac{1}{R_1} + \frac{1}{R_2}\right) \approx \sigma\left(\frac{2\cos(\pi-\theta)}{L} + \sqrt{\frac{\pi L}{V}}\right) \tag{2.2}$$

where σ is the surface tension coefficient of the liquid-air interface, R_1 and R_2 are the curvature radii of the liquid-air interface, L is the gap distance between the actuation plate and the substrate, θ is the contact angle of the liquid on solid surfaces, and V is the liquid volume.

The force induced by the Laplace pressure in the vertical direction is

$$F_p = PS = \sigma \left(\frac{2\cos(\pi - \theta)}{L} + \sqrt{\frac{\pi L}{V}} \right) \cdot \frac{V}{L} \approx \sigma \left(\frac{-2\cos\theta}{L^2} V + \sqrt{\frac{\pi V}{L}} \right) \quad (2.3)$$

The surface tension along the vertical direction is

$$F_s \approx 2\pi R_2 \sigma \sin(\pi - \theta) \approx 2\sigma\pi \sqrt{\frac{V}{\pi L}} \sin\theta \quad (2.4)$$

The total force in the vertical direction is

$$F_s = 2\sigma\pi \sqrt{\frac{V}{\pi L}} \sin\theta - \sigma \frac{-2\cos\theta}{L^2} V - \sigma \sqrt{\frac{\pi V}{L}} \quad (2.5)$$

Experiment is performed to validate the simulation result for the force produced by the liquid interface in the film state, as shown in figure 2.6. The simulation result agrees with the experimental result very well, which indicates that the analytic model is precise. Moreover, when the total gap distance is small the total force is negative, meaning the total force is repulsive. The total force comprises the surface tension and the Laplace pressure. The surface tension is attractive; the Laplace pressure is attractive when the curvature of the liquid bridge is negative and repulsive when it is positive. When the gap decreases to a small value, the Laplace pressure is dominant, and because the curvature of the liquid bridge is positive, the total force is repulsive.
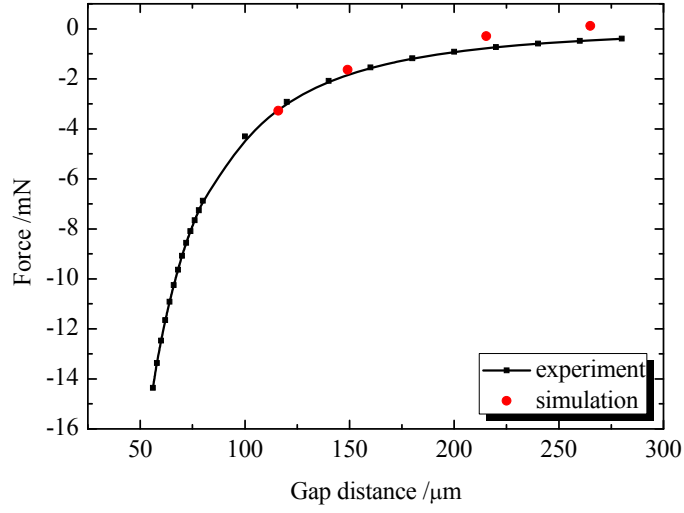
Figure 2.6 Experimental validation of the simulation result for the capillary force produced by the liquid interface in the film state: negative sign means the total force is repulsive

Figure 2.7 shows the capillary forces produced by the liquid interfaces in the film state when the liquid volumes are 0.10 μL, 0.17 μL and 0.24 μL, which are the same liquid volumes used in the thermally and mechanically coupled mathematical model. It reveals that a larger liquid volume results in a larger capillary force for a constant gap distance, and when the gap distance is decreased, the difference becomes more pronounced. This effect can be explained using equation 2.5. When the gap distance is small, the second term in equation 2.5 dominates the total force, as shown in equation 2.6. Equation 2.6 indicates that the total force increases as the liquid volume increases, and the negative sign indicates that the total force is repulsive.
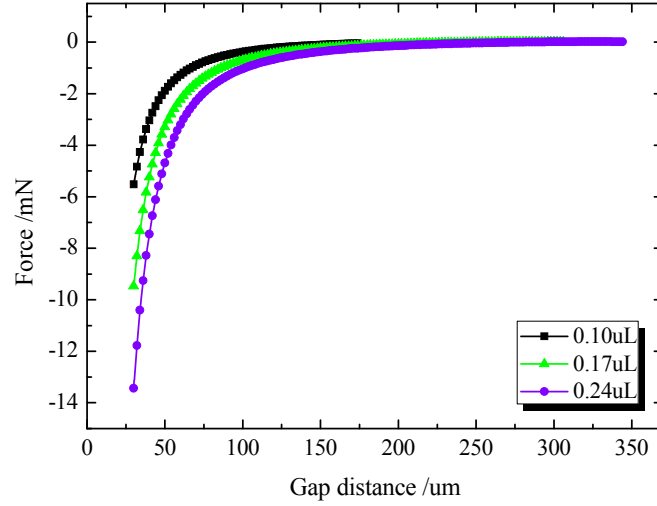
$$F_t = -\sigma \frac{-2\cos\theta}{L^2}V \qquad (2.6)$$

Figure 2.7 Comparison of capillary forces produced by liquid interfaces with different liquid volumes of 0.10 µL, 0.17 µL, and 0.24 µL in the film state

A mathematical model built with Surface Evolver is used to calculate the capillary force produced by the liquid interface in the droplet state. Surface Evolver is an interactive computer program for the study of surfaces affected by surface tension and other energies. It evolves the surface down the energy gradient under certain constraints to minimize the energy of the surface. Figure 2.8 shows the surface morphology of a liquid droplet obtained using Surface Evolver. The surface is represented as a simplicial complex. Table 2.1 shows that the rupture distance of the liquid bridge increases as the liquid volume increases according to the simulation results.
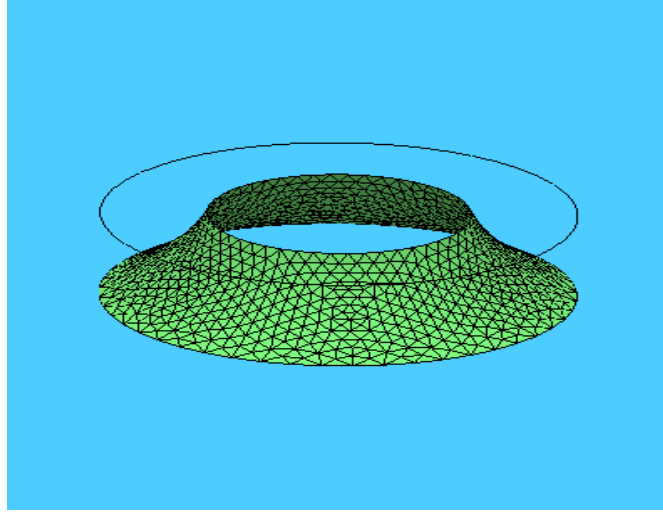
Figure 2.8 Surface morphology of a liquid droplet obtained using Surface Evolver

Table 2.1 Rupture distances of the liquid bridges with different liquid volumes

predicted by the Surface Evolver model

Parameter	Volume1	Volume2	Volume3
volume/ μL	0.10	0.17	0.24
rupture distance/ mm	0.305	0.436	0.509

2.4 Magnetic force

The magnetic force is measured and fitted as is described in the literature [16], as shown in figure 2.9. The expression of the fit is presented in equation 2.7 [16]. However, the gadolinium plate used to measure the magnetic force is not available for use in the experimental setup of the thermal energy harvester. Therefore, the magnetic forces are measured at several points using the current experimental setup of the thermal energy harvester to validate equation 2.7, as shown in table 2.2. Table 2.2 shows that the

magnetic force according to equation 2.7 should be reduced by approximately 10% to fit
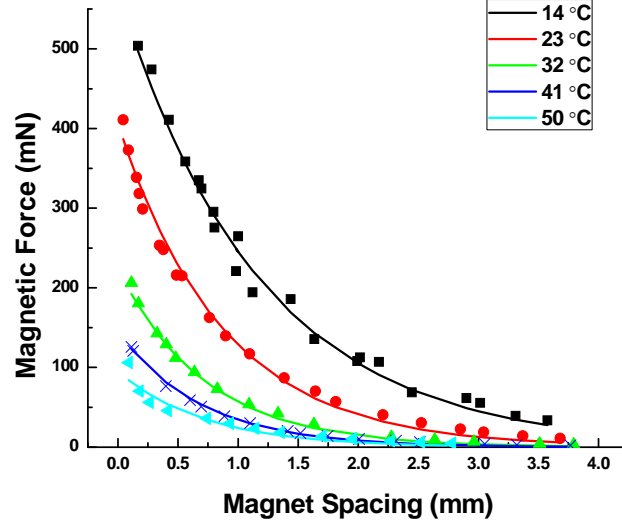
the actual value.

Figure 2.9 Experimental and analytical fit for the magnetic force vs. the magnet

spacing for different gadolinium temperatures. The dots represent the experimental

data, and the lines represent the modeling fit. [16]

$$F_{mag} = ae^{bx};$$
$$a = -0.01218T^4 + 0.1612T^3 - 7.26T^2 + 114.1T + 2.875; \qquad (2.7)$$
$$b = \left(-8.12 \cdot 10^{-9}\right)T^4 + 0.0001088T^3 - 0.004364T^2 + 0.03528T - 0.7533;$$

Table 2.2 Comparison of the magnetic forces according to the experimental

measurement and the expression of the fitting curve

Parameter	Point1	Point2	Point3
position/ mm	0.788	0.732	0.676
measuring data/ mN	151.9	160.0	169.7
modeling data	170.9	182.1	194.1
measurement/model	0.89	0.88	0.87
model-measurement	18.996	22.12	24.42

Chapter3. Modeling validation and investigation

3.1 Introduction

In this chapter, a coupled thermal and mechanical model is used to optimize the design of a thermal energy harvester with a reversible liquid interface. The simulation results are validated with experimental results, confirming that the model can correctly predict the behaviors of the device with reasonable levels of accuracy.

3.2 Model description

A mathematical model has been developed that simultaneously solves coupled thermal and mechanical equations for a thermal energy harvester without a reversible liquid interface by Bulgrin [16, 17]. This mathematical model is improved to include the reversible liquid interface.

There are a total of four forces exerted on the actuation plate: the spring force, the magnetic force, the gravitational force, and the capillary force. Among these four forces, the interplay of the two main forces results in the oscillation of the actuation plate as follows: the spring force brings the actuation plate up to the surface of the heat sink, and the magnetic force between the permanent magnet and the gadolinium plate brings the actuation plate down to the surface of the heat source. When the liquid bridge connecting the actuation plate and the hot surface has a positive curvature and the Laplace pressure dominates over the surface tension, the liquid interface provides a repulsive force to repel

the actuation plate. The minimum thickness of the liquid film is determined by the force balance of the four forces. However, if the surface tension dominates over the Laplace pressure, the liquid interface provides an attractive force to pull the actuation plate down.

The total force in the vertical direction is given by

$$F_{tot} = F_{spr} + F_{mag} + F_{gra} + F_{cap} \tag{3.1}$$

where F_{spr} is the spring force, F_{mag} is the magnetic force, F_{gra} is the gravitational force, and F_{cap} is the capillary force. The spring force can be calculated with Hooke's law, and the magnetic force is modeled by creating an analytical fit of the experimental data. The capillary forces are calculated differently for different liquid states: in the droplet state, the capillary force is calculated with an analytical fit of the simulation data from the Surface Evolver model, and in the film state, the capillary force is calculated with the analytical model. The methods to calculate and validate the three forces are discussed in detail in chapter 2.

The position of the actuation plate can be calculated by Newton's second law [16, 17]

$$m_{pl} \frac{d^2 x}{dt^2} = F_{tot} \tag{3.2}$$

where m_{pl} is the mass of the actuation plate.

When the gadolinium plate is heated by the heat source or cooled by the heat sink, a lumped capacitance model is used to calculate the temperature. The heat transfer via radiation and convection is neglected to simplify the mathematical model. The temperature of the gadolinium plate is determined by the following equation [16, 17]

$$m_{Gd} \cdot c_p \cdot \frac{dT}{dt} = \left(T_{hs/cs} - T \right) \cdot C_c \cdot A_{Gd} \qquad\qquad (3.3)$$

where m_{Gd}, c_p, and A_{Gd} are the mass, the specific heat and the area of the gadolinium plate, respectively, and C_c is the thermal contact conductance between the gadolinium and the cold surface or the thermal contact conductance of the liquid interface.

It is difficult to model the thermal contact conductance of the liquid interface because the morphology of the liquid bridge changes with the position of the actuation plate. However, heat transfer through the liquid bridge occurs mainly when a thin layer of liquid film is formed because this morphology has a larger thermal conductance. It is therefore assumed that the thermal contact conductance of the liquid interface is the value when the liquid interface achieves its minimum thickness

$$C_{c,l} = \sigma \frac{S}{L} = \sigma \frac{V}{L^2} \qquad\qquad (3.4)$$

where σ is the thermal conductivity of the liquid, V is the liquid volume, and L is the minimum thickness of the liquid film.

The force balance equation, given in equation 3.1, for the position at the cold surface is first solved to obtain the cold actuation temperature, which is the temperature of the gadolinium plate when it leaves the cold surface. With the cold actuation temperature as a known parameter, equation 3.1 is solved for a position near the hot surface to obtain the minimum thickness of the liquid film. Then, the coupled thermal and mechanical equation group is solved simultaneously using Euler's method to predict the position and temperature of the gadolinium plate. Finally, the oscillation frequency of the device is calculated.

3.3 Model validation

The minimum thickness of the liquid film predicted by the model is in agreement with the experimental result, as shown in figure 3.1. This agreement indicates that the mathematical model is able to accurately predict the minimum thickness of the liquid interface. As shown in this figure, a larger liquid volume results in a larger minimum thickness of the liquid film because a larger liquid volume produces a larger capillary force, as demonstrated in figure 2.8d. Figure 3.2 shows that a larger liquid volume leads to a larger maximum area of the liquid film, and table 3.1 presents the modeled thermal conductance and the experimental thermal conductance for different liquid volumes. The results of both the model and the experiment indicate that the thermal conductance of the liquid interface decreases with increasing liquid volume because the minimum thickness of the liquid film increases with increasing liquid volume and that the thermal conductance dominates over the liquid volume in equation 3.4.
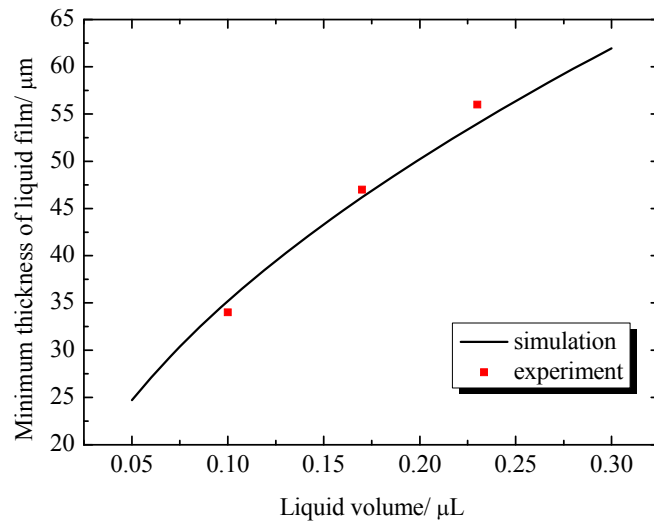
Figure 3.1 Comparison of the minimum thicknesses of the liquid film determined by the model and the experiment for different liquid volumes
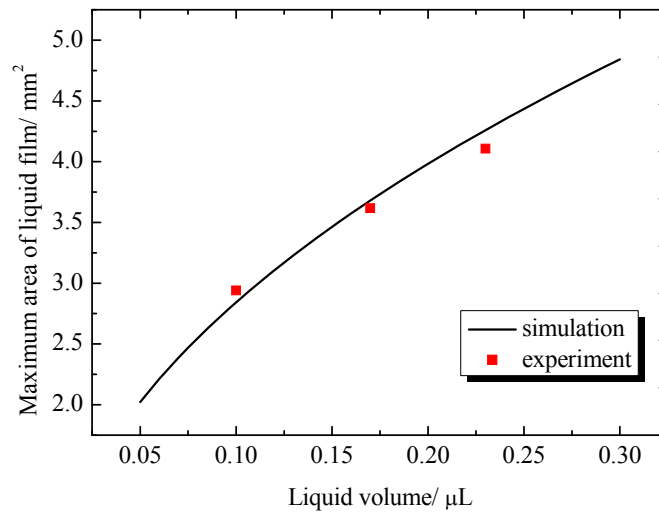

Figure 3.2 Comparison of the maximum areas of the liquid film determined by the model and the experiment for different liquid volumes

**Table 3.1 The thermal conductances determined by the model and the experiment for different liquid volumes**

Parameter	Volume1	Volume2	Volume3
Volume/μL	0.10	0.17	0.23
thermal conductance of simulation (W/K)	0.0485	0.0478	0.0474
thermal conductance of experiment (W/K)	0.0519	0.0462	0.0440

The modeled oscillation frequency and the hot residence time are validated by three groups of experimental results for different total gap distances, as shown in figures

3.3, 3.4 and 3.5. The modeled oscillation frequency exhibits a trend similar to that of the experimental results, and these two results are nearly in agreement, which indicates that the model is able to serve as a tool to evaluate the performance of the device. The hot residence time determined by the model is in agreement with the experimental result, which proves that the simplification used to calculate the thermal conductance of the liquid interface is reasonable and acceptable.
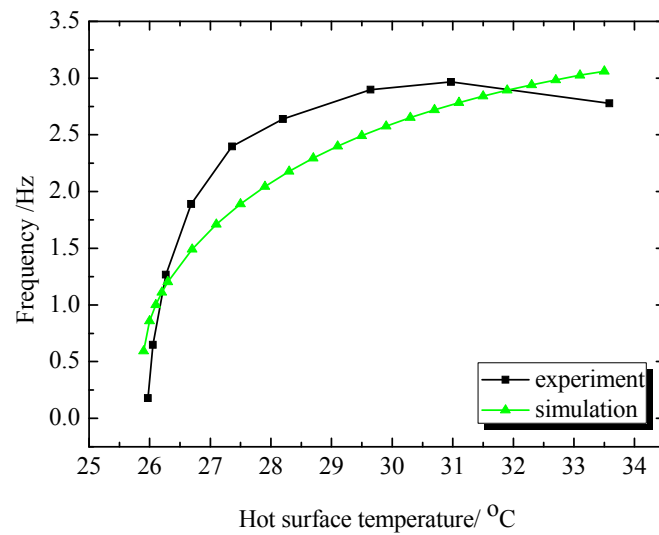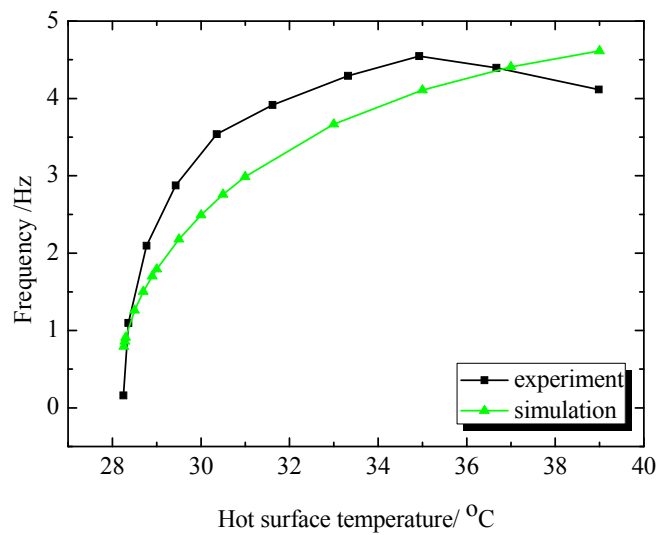

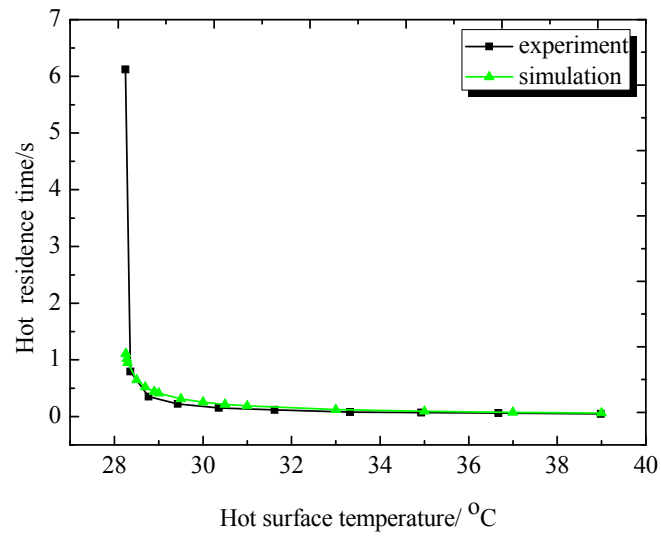**(a) Oscillation frequency vs. hot surface temperature**
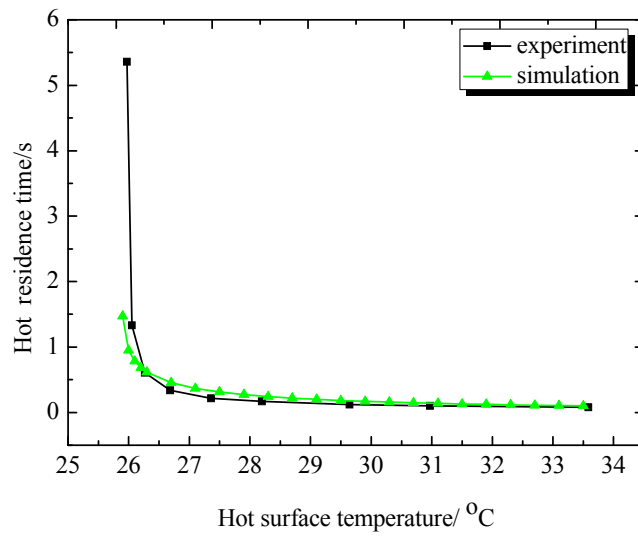
(b) Hot residence time vs. hot surface temperature

Figure 3.3 Comparison of the frequencies and the hot residence times determined by the model and the experiment when the total gap distance is 1.40 mm: (a) oscillation frequency vs. hot surface temperature; (b) hot residence time vs. hot surface temperature
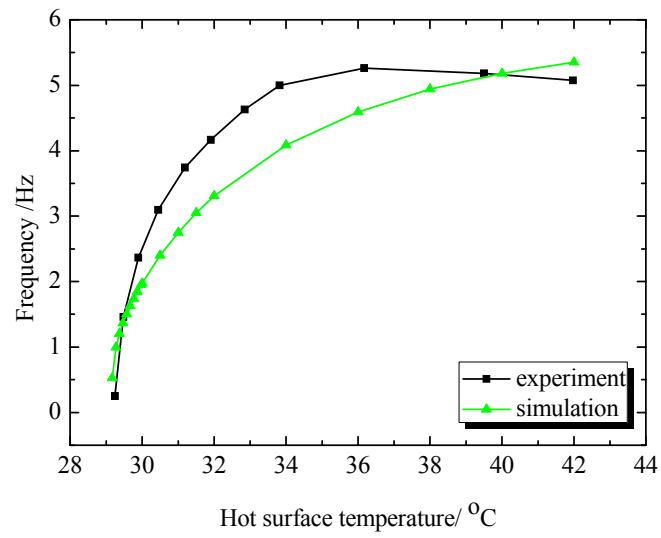
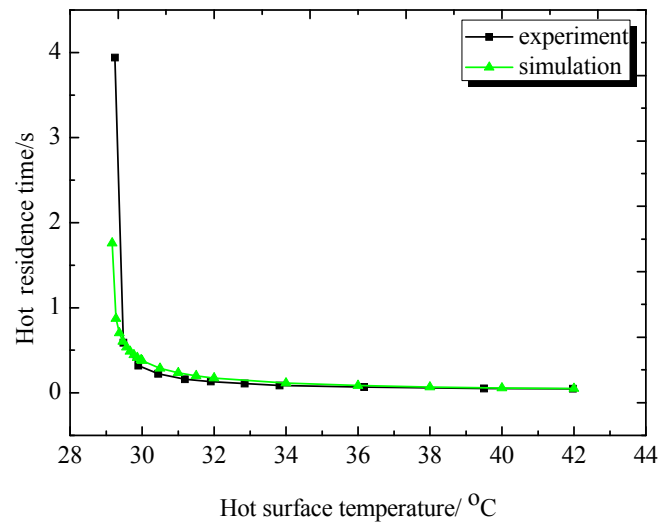**(a) Oscillation frequency vs. hot surface temperature**

(b) Hot residence time vs. hot surface temperature

Figure 3.4 Comparison of the frequencies and the hot residence times determined by the model and the experiment when the total gap distance is 1.28 mm: (a) oscillation frequency vs. hot surface temperature; (b) hot residence time vs. hot surface temperature

(a) Oscillation frequency vs. hot surface temperature

(b) Hot residence time vs. hot surface temperature

Figure 3.5 Comparison of the frequencies and the hot residence times determined by the model and the experiment when the total gap distance is 1.21 mm: (a) oscillation frequency vs. hot surface temperature; (b) hot residence time vs. hot surface temperature

3.4 Modeling investigation

As shown in figure 3.6, the results predicted by the mathematical model indicate that the oscillation frequency of the device increases as the volume of the liquid interface increases. This is because a smaller liquid volume results in a larger thermal contact conductance between the gadolinium and the hot surface, as presented in table 3.1. Thus, the time required to heat the gadolinium is reduced and the oscillation frequency of the device is increased.
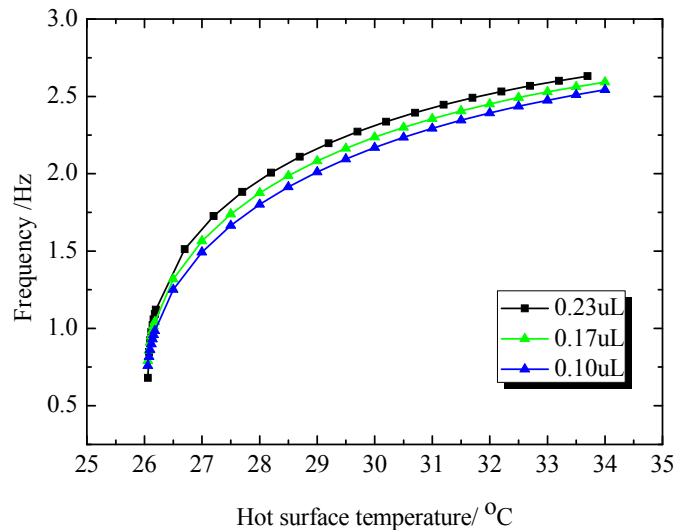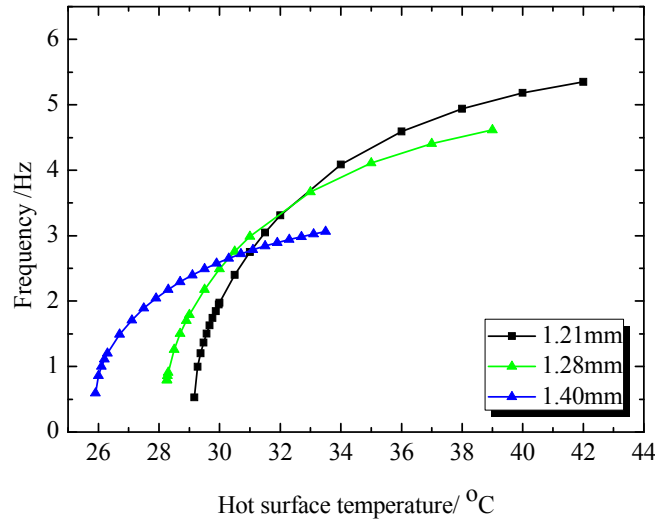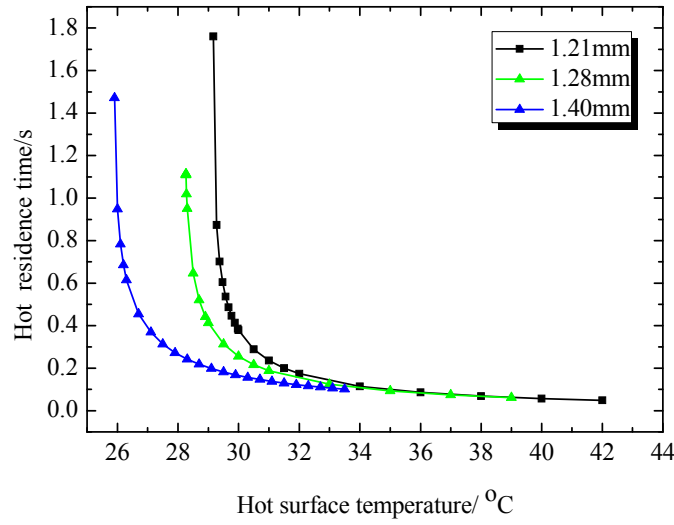
Figure 3.6 Oscillation frequency vs. hot surface temperature for different liquid volumes. For all three simulations, the other parameters were kept constant, with the exception of the liquid volume

The total gap distance is also optimized with the mathematical model. An optimized liquid volume, 0.08 µL, is used in the simulations. As shown in figure 3.7a, the oscillation frequency of the device increases as the total gap distance decreases because the difference between the hot actuation temperature and the cold actuation temperature decreases as the total gap distance decreases. Therefore, the gadolinium requires less time to be heated at the hot side or cooled at the cold side. This explanation is confirmed by figure 3.7b, which shows that the hot residence time decreases as the total gap distance decreases. In addition, a small total gap distance also requires a small liquid volume; otherwise, the liquid bridge cannot rupture.

(a) Oscillation frequency vs. hot surface temperature

(b) Hot residence time vs. hot surface temperature

Figure 3.7 Modeling prediction of the effects of different total gap distances on the oscillation frequency and the hot residence time: (a) oscillation frequency vs. hot surface temperature; (b) hot residence time vs. hot surface temperature. In the three simulations, all parameters except total gap distance are kept constant.

Using the optimized liquid volume and total gap distance parameters, the cold surface temperature is further optimized to maximize the oscillation frequency, as shown in figure 3.8. Figure 3.8 shows that the device achieves a higher oscillation frequency at a lower cold surface temperature because the gadolinium requires less time to be cooled at the cold side when the cold surface temperature is lower.
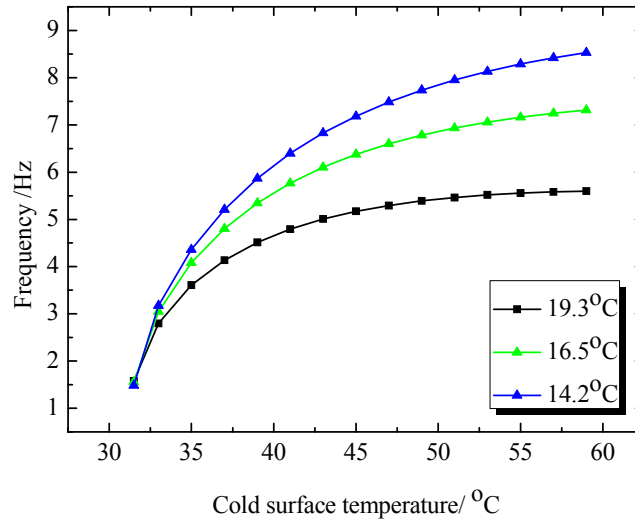
Figure 3.8 Modeling prediction of the effects of different cold surface temperatures on the oscillation frequency of the device. In the three simulations, all parameters except liquid volume are kept constant.

In conclusion, the oscillation frequency is the parameter used to evaluate the performance of the device, the results predicted by the mathematical model lead to the following conclusions: a liquid interface with a smaller liquid volume is preferred because it results in a larger thermal contact conductance and a smaller rupture distance, a smaller total gap distance is preferred because it reduces the time required for the gadolinium to be heated on the hot surface and cooled on the cold surface, and a lower cold surface temperature is preferred because it reduces the time required for the gadolinium to be cooled on the cold surface.

Chapter 4. Experimental setup and investigation

4.1 Introduction

In this chapter, a thermal energy harvester with a reversible liquid interface is physically built. The device is constructed step by step according to the optimized results obtained from the mathematical model. Experiments are performed to evaluate the effect of the reversible liquid interface on the oscillation frequency of the device. The experimental results are also used to validate the predictions made by the mathematical model.

4.2 Experimental setup

The experimental setup of the device is illustrated in figure 4.1. Two Peltier devices are stacked together to act as a cooling pump to cool the cold surface. The hot side of the top Peltier device is attached to a small fan to remove the excess thermal energy and prevent burning of the Peltier devices. The temperature of the cold surface is controlled by adjusting the power supplies of the Peltier devices and the fan. The gadolinium plate is attached to the central region of the actuation plate of the spring frame with a strong adhesive. The cooling surface and the spring frame are then fixed on an adjustable stage such that the total gap distance is controlled by adjusting the stage. For the hot side, a ceramic heater with an area of 1 cm×1 cm is used as the heat source. The temperature of the hot surface is then controlled by the power supply of the heater. A

permanent magnet is attached to the heater with thermal grease. The ceramic heater and the permanent magnet are then packaged with room temperature vulcanized rubber to reduce the heat dissipation. A digital camera is used to record the oscillating motion of the actuation plate, and a light-emitting diode is used to illuminate the device for the camera.
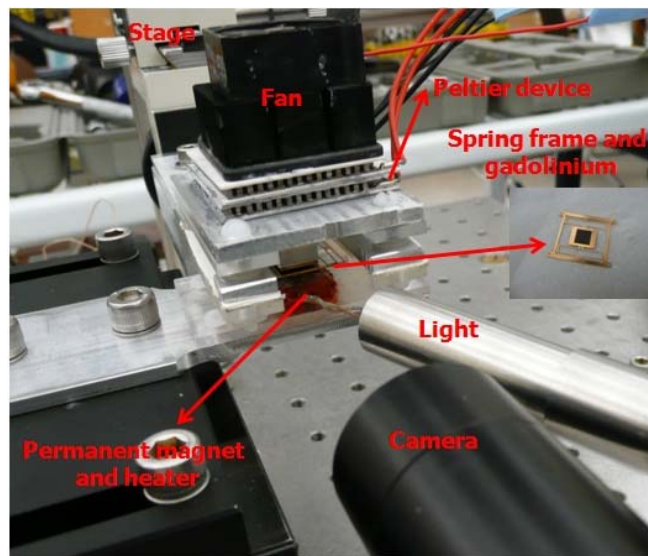

Figure 4.1 Experimental setup of the device

A self-developed fabrication method is used to fabricate a hydrophilic pattern on a Teflon-coated silicon substrate for the reversible liquid interface, as illustrated in figure 4.2. First, a PDMS column is molded with a plastic glass plate as the mold. PDMS is an important polymer material that is widely used in microfluidics and BioMEMS. Second, the PDMS column is attached to a silicon substrate using the innate adhesive characteristics of PDMS. The Teflon solution is then painted onto the silicon substrate

with a brush. Finally, the PDMS column is peeled off, revealing the resultant hydrophilic pattern on the substrate.

According to the traditional fabrication method [25, 26], a layer of Teflon is spin-coated onto a substrate and then a photoresist is used as a mask. Reactive ion etching (RIE) is then used to create the pattern. Because of the hydrophobicity of Teflon, spin-coating a layer of photoresist onto the Teflon layer is somewhat difficult. Thus, a brief RIE step is generally used to roughen the surface of the Teflon to improve the adhesion of the photoresist onto the Teflon layer. However, this roughening compromises the surface hydrophobicity of the Teflon layer. Compared with the traditional method, the method developed in this work has the following advantages: it does not compromise the surface hydrophobicity of the Teflon layer, requires less time and is relatively simple and inexpensive because no clean room is required. A fabricated sample is shown in figure 4.3, and the pattern is a nearly perfect circle. Figure 4.4 shows a liquid droplet that is initially confined within the pattern.

(a) Molding a PDMS column
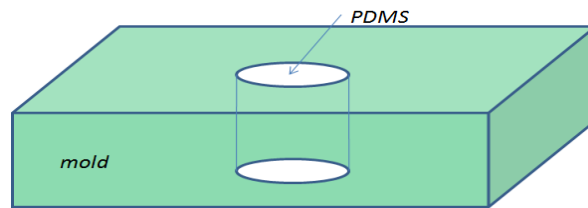
(b) Painting the Teflon solution
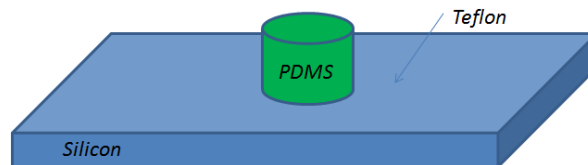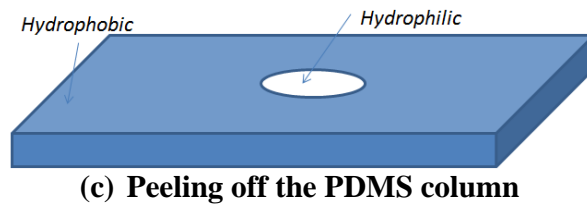
(c) Peeling off the PDMS column

Figure 4.2 Steps required to fabricate a pattern on a silicon substrate for the liquid interface: (a) molding a PDMS column; (b) painting the Teflon solution; (c) pattern remaining on the substrate after the PDMS column is removed
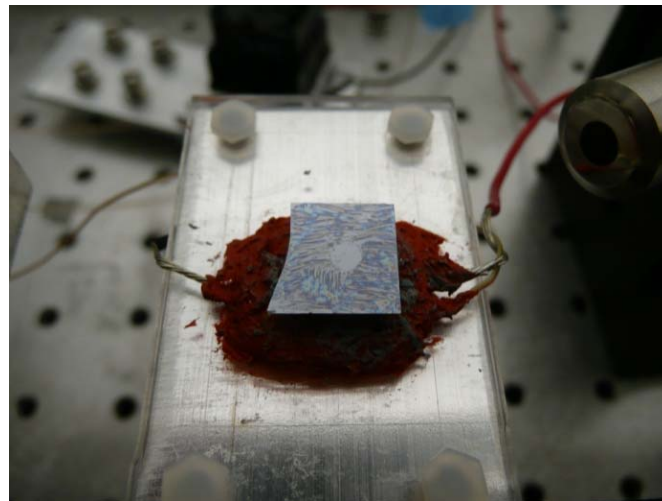

Figure 4.3 Photograph of the fabricated sample revealing that the pattern is a nearly perfect circle
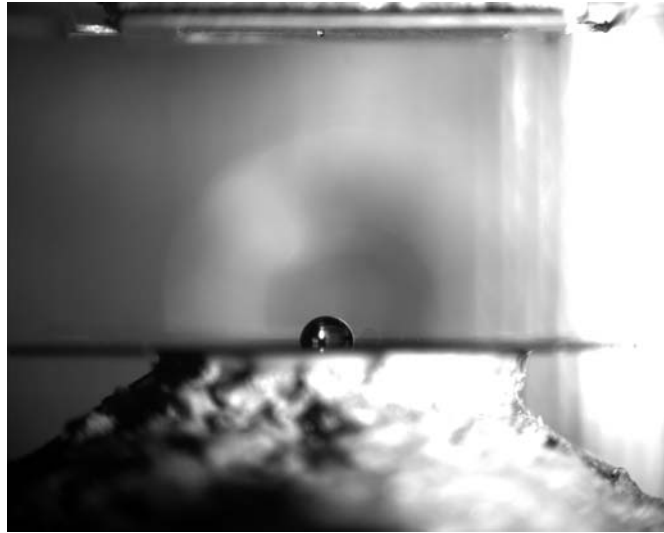
Figure 4.4 A liquid droplet initially confined within the hydrophilic area

4.3 Experimental investigation

The experimental results indicate that the reversible liquid interface can effectively improve the oscillation frequency of the device in the low-temperature region, as presented in figure 4.5. These results prove that the reversible liquid interface can achieve a larger thermal contact conductance than the direct solid-solid contact interface. Therefore, the gadolinium requires a shorter time to be heated on the hot surface, as illustrated in the low-temperature portion of figure 4.6. Figure 4.6 also shows that the reduction of the hot residence time decreases as the hot surface temperature is increased due to the larger temperature difference between the gadolinium and the hot surface. Therefore, the improvement in the oscillation frequency is decreased.

However, figure 4.5 shows that the oscillation frequencies achieved when liquid interfaces are used are lower than the oscillation frequency when no liquid interface is

used in the high-temperature region. The videos of the experiments show that there is some liquid attached to the gadolinium surface that are possibly due to defects on the gadolinium surface, which will be discussed in appendix A. The liquid attached to the gadolinium surface increases the time required for heating and cooling the gadolinium. The increased time due to the attached liquid is greater than the time saved by using the liquid interface. Therefore, the oscillation frequency is decreased. Another possible reason is that the liquid interface results in more severe air conduction.

Moreover, figure 4.5 shows that a liquid interface with a smaller volume increases the oscillation frequency of this device except in the low-temperature region. This result is in general agreement with the prediction made by the mathematical model. In the low-temperature region of figure 4.5, a larger liquid volume results in a lower "turn-on" temperature for the device because the liquid interface with a larger volume has a longer rupture distance, which leads to a smaller total gap distance and therefore a higher "turn-on" temperature for the device. This phenomenon is not clearly observable in the simulations because the liquid bridge is modeled as a thin layer of liquid film for heat transfer and the minimum thickness of the liquid film (~tens of microns) is negligible compared to the total gap distance (~1-2 mm).
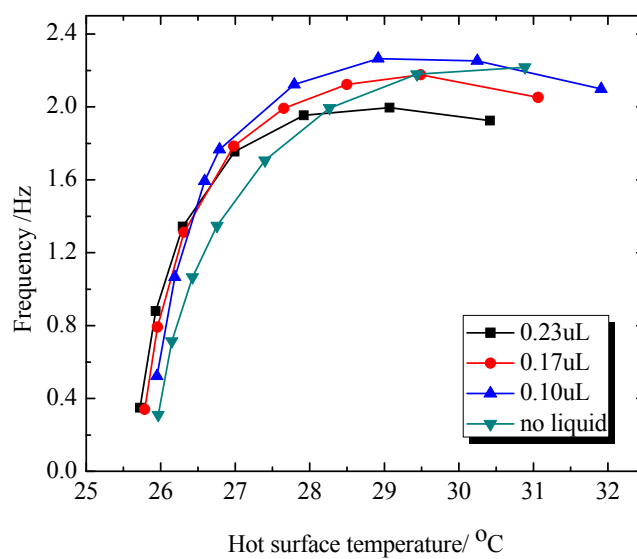
Figure 4.5 Experimental oscillation frequency vs. hot surface temperature for different liquid volumes. The total gap distance is 1.46 mm, and the cold surface temperature is 15.5°C
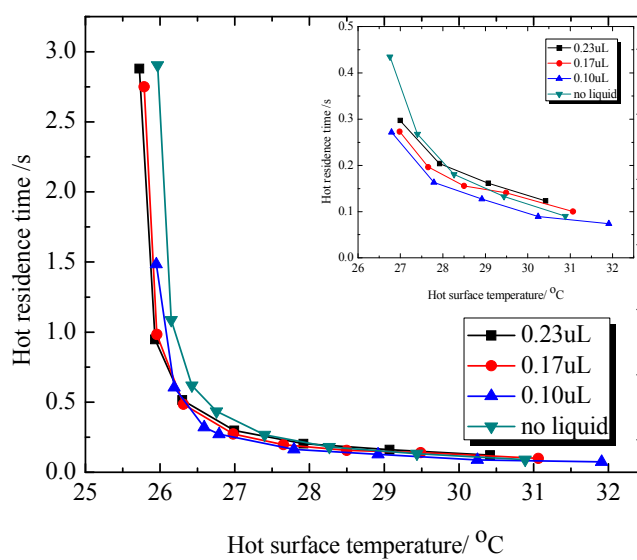
Figure 4.6 Experimental hot residence time vs. hot surface temperature for different liquid volumes. The inset shows the high-temperature region of the large figure. The total gap distance is 1.46 mm, and the cold surface temperature is 15.5°C

The equation of the lumped capacitance model (equation 3.3) can be solved to get the solution of the hot residence time, as shown in the following expression

$$t_{hot} = \frac{m_{Gd}c_p}{C_l A_{Gd}} \ln \frac{T_{ca} - T_{hs}}{T_{ha} - T_{hs}} = k \ln \frac{T_{ca} - T_{hs}}{T_{ha} - T_{hs}} \tag{4.1}$$

where term $\ln \dfrac{T_{ca} - T_{hs}}{T_{ha} - T_{hs}}$ is called as the temperature parameter, k is the slope of the curve of the hot residence time versus the temperature parameter.

Therefore, the effective thermal contact conductance of the liquid interface can be written as

$$C_l = \frac{m_{Gd}c_p}{kA_l} \tag{4.2}$$

Equation 4.2 indicates that the effective thermal contact conductance of the liquid interface is inversely proportional to the slope k.

Figure 4.7a shows that the hot residence time first linearly increases as the temperature parameter increases, and then increases rapidly when the temperature parameter becomes larger. This result indicates that the effective thermal contact conductance of the liquid interface is not a constant, and increases as the hot surface temperature increases. This is because that the loading pressure of the gadolinium plate varies when its temperature changes, and thus the thickness and the thermal contact

conductance of the liquid interface changes over time. When the hot surface temperature is high, the gadolinium plate can be heated very quickly, therefore, the heat transfer process is able to finish before the liquid interface becomes thick, resulting in a larger and constant effective thermal contact conductance. This explanation is confirmed by figure 4.7b.

The effective thermal contact conductance of the liquid interface at high hot surface temperatures is approximately estimated with figure 4.7b, and it should be close to the maximum thermal contact conductance of the liquid interface. This conclusion is confirmed by table 4.1. Table 4.1 also shows that the effective heat transfer coefficients when liquid interfaces are used are much larger than that when no liquid interface is used. This result indicates that if the maximum area of the liquid interface can be increased without increasing the minimum thickness of the liquid interface, the oscillation frequency of the device can be further improved.
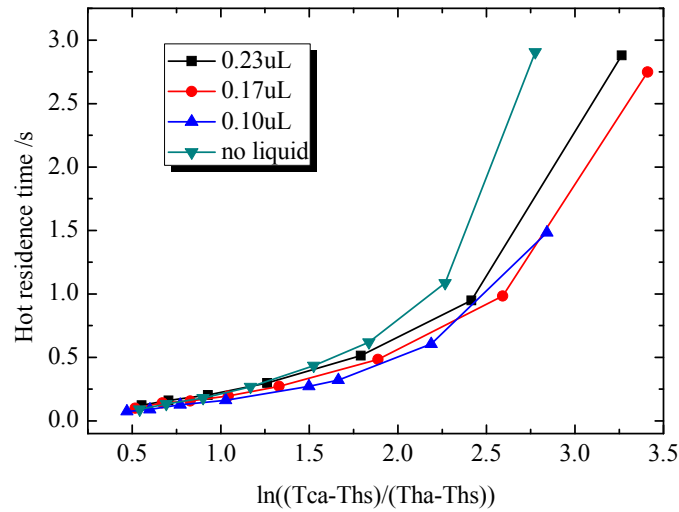
(a)
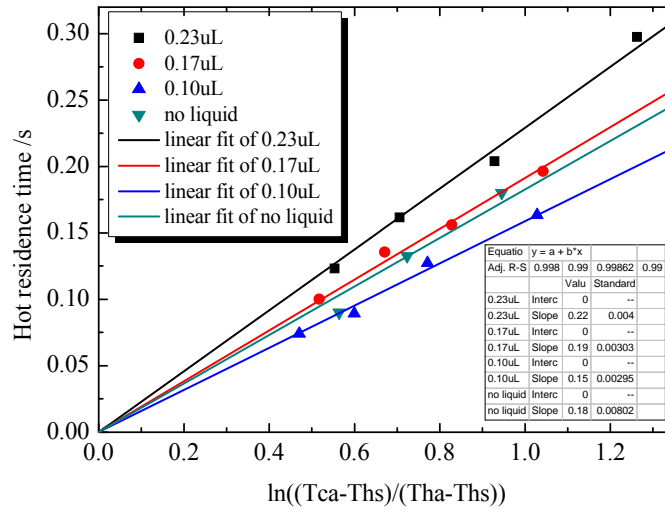
(b)

Figure 4.7 Experimental hot residence time vs. temperature parameter for different liquid volumes. Figure (b) is the beginning region of figure (a). A low hot surface temperature corresponds to a higher hot surface temperature

Table 4.1 Comparison of the effective thermal conductances and the maximum thermal conductances of the liquid interfaces for different liquid volumes

Parameter	Volume1	Volume2	Volume3	No liquid
Volume/μL	0.10	0.17	0.23	××
effective thermal conductance (W/K)	0.0519	0.0430	0.0359	0.0443
effective heat transfer coefficient (W/m^{2}K)	17642	11921	8750	1230
maximum thermal conductance (W/K)	0.0519	0.0462	0.0440	××
maximum heat transfer coefficient (W/m^{2}K)	17647	12766	10714	××

42

The oscillation frequency of the device can be further improved by optimizing the total gap distance, as shown in figure 4.8. Figure 4.8 shows that the maximum oscillation frequency increases as the total gap distance decreases because the difference between the hot actuation temperature and the cold actuation temperature decreases. Thus, both the hot residence time and the cold residence time are reduced, as presented in figure 4.8 for the hot residence time.

Figure 4.9 shows that the reduction of the hot residence time decreases as the hot surface temperature decreases, similar to the trend observed in figure 4.6. At high surface temperatures, the differences of the hot residence times for different total gap distances are almost negligible while the differences in the frequencies are clear. This result indicates that the cold residence time dominates over the hot residence time for a single period of oscillation at high temperature. Thus, use of the liquid interface achieves a limited increase in the oscillation frequency at high hot surface temperatures.
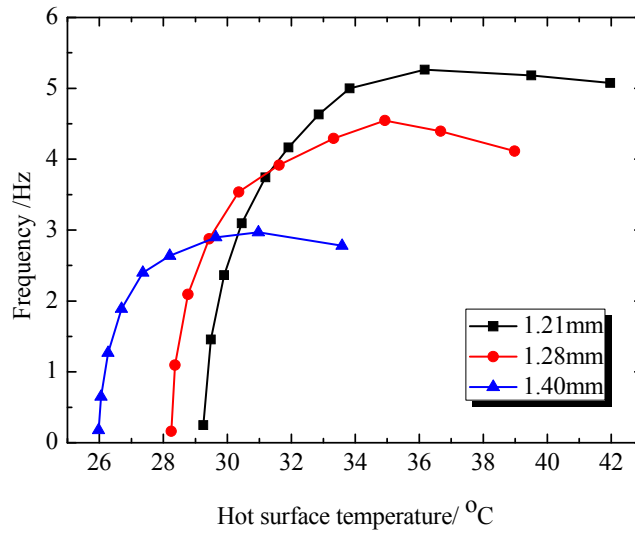
Figure 4.8 Experimental oscillation frequency vs. hot surface temperature for different gap distances. The liquid volume is 0.08 μL, and the cold surface temperature is 15.5^{o}C
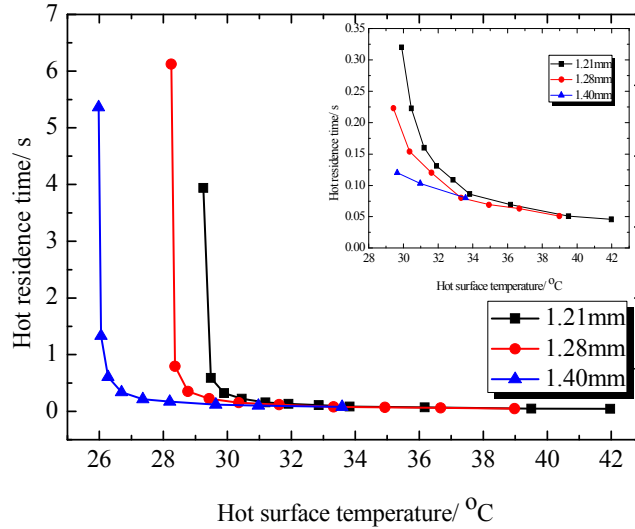

Figure 4.9 Experimental hot residence time vs. hot surface temperature for different gap distances. The inset shows the high-temperature regionof the large figure. The liquid volume is 0.08 μL, and the cold surface temperature is 15.5^{o}C

In addition to optimizing the liquid volume and the total gap distance, the oscillation frequency of the device can be further increased by optimizing the cold surface temperature, as shown in figure 4.10. The device achieves a higher oscillation frequency at a lower cold surface temperature because the lower cold surface temperature reduces the cold residence time. The maximum oscillation frequency is approximately 8.3Hz and is achieved at a hot surface temperature of 41.8^{o}C. However, decreasing the cold surface temperature beyond this point results in some issues. One issue is that water

condensation can occur on the cold surface, which leads to the failure of the device operation. Furthermore, a lower cold surface temperature results in an increase of the hot residence time, as presented in figure 4.11, because the effects of air conduction, which cools the gadolinium at the hot side, become significant.
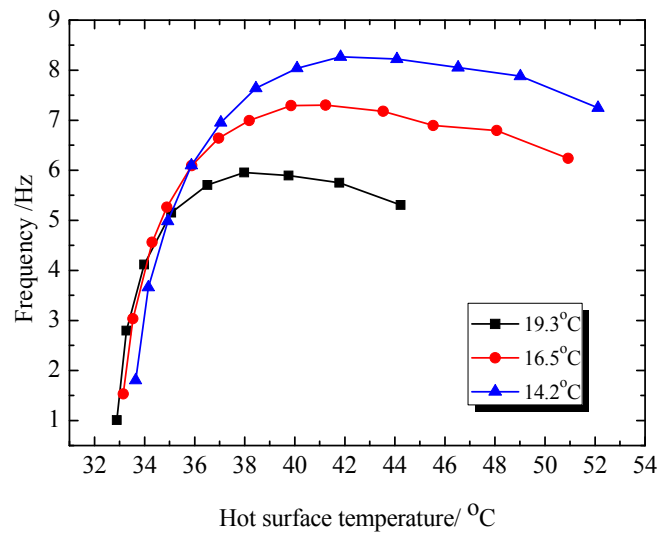

Figure 4.10 Experimental oscillation frequency vs. hot surface temperature for different cold surface temperatures. The total gap distance is 1.08 mm, and the liquid volume is 0.06 µL
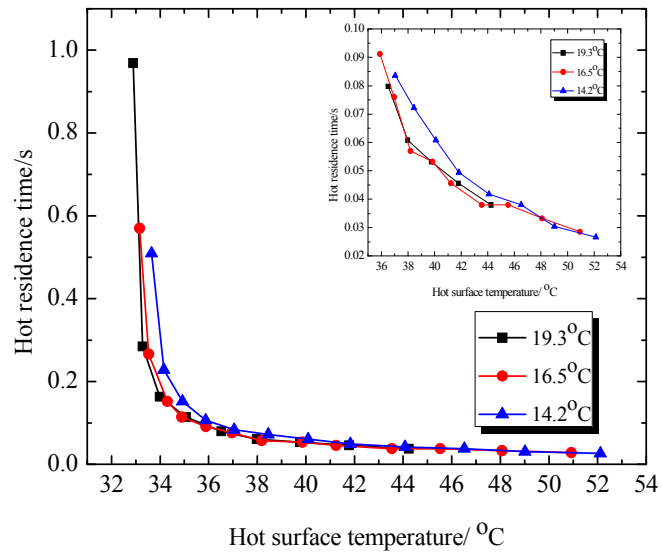
Figure 4.11 Experimental hot residence time vs. hot surface temperature for different cold surface temperatures. The inset shows the high-temperature region of the large figure. The total gap distance is 1.08 mm, and the liquid volume is 0.06 µL

Chapter 5. Conclusions

In this thesis, a thermal energy harvester using a ferromagnetic material with a reversible liquid interface is investigated. Simulations are performed to optimize the design of the device using a coupled thermal and mechanical mathematical model. The device is physically built, and its performance is evaluated.

The experimental results for the spring constant, the capillary force and the magnetic force are in agreement with the calculated results, indicating that the estimations of the three parameters are precise. The calculated results show that the reversible liquid interface with a larger liquid volume yields a larger repulsive force and a longer rupture distance.

The modeling results are in agreement with the experimental results, indicating that the model can correctly predict the behaviors of the device with reasonable levels of accuracy. The model predicts that a smaller liquid volume, a smaller total gap distance and a lower cold surface temperature are preferred to maximize the oscillation frequency of the device.

The experimental results confirm that the reversible thermal interface can effectively improve the oscillation frequency in the low hot surface temperature region. Using the optimized design predicted by the mathematical model, the device achieves a maximum oscillation frequency of 8.3Hz at a hot surface temperature of 41.8°C.

In the current device, the reversible thermal interface is only exploited on the hot surface to improve the thermal contact conductance between the gadolinium and the hot surface. In fact, a reversible thermal interface could also be adopted on the cold surface to

improve the thermal contact conductance between the gadolinium and the cold surface. Because the cold residence time dominates at higher hot surface temperatures, a reversible thermal interface on the cold surface will further improve the oscillation frequency in the high hot surface temperature region.

This thesis only presents the prototype of a device that can oscillate properly. In future work, piezoelectric materials and pyroelectric materials will be exploited in the device to convert the mechanical energy and the temperature polarizations into electrical energy.

Appendix A: Hydrophobicity of the Teflon-coated gadolinium surface

Gadolinium is relatively stable in dry air. However, it tarnishes quickly when moisture is present and a loosely adhering gadolinium oxide (Gd_2O_3) is formed, as described by the following equation [27]

$$4Gd + 3O_2 \rightarrow 2Gd_2O_3 \tag{A.1}$$

Gadolinium oxide can react with hydrogen chloride to form the salt $GdCl_3$, which is a colorless, hygroscopicand water-soluble solid [28], through the reaction shown in the following equation

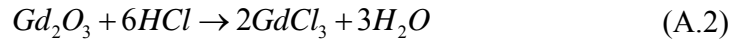$$Gd_2O_3 + 6HCl \rightarrow 2GdCl_3 + 3H_2O \tag{A.2}$$

Figure A.1 shows images of three gadolinium surfaces subjected to different treatments that were obtained using an optical microscope with 10x magnification. Figure A.1a shows the original gadolinium surface. The loosely adhering gadolinium oxide creates defects on the gadolinium surface, which can pin the contact line of a droplet [29]. Figure A.1b shows the gadolinium surface after polishing. The gadolinium was polished with an abrasive paper to obtain a smooth surface. There are some scratches on the surface that may also result in defects. Figure A.1c shows the gadolinium surface after reaction with hydrogen chloride. A solution of 2 M hydrogen chloride was used to treat the gadolinium, and the reaction time was approximately 1-2s. The gadolinium oxide was not completely removed, and the surface became rougher than the original surface. One

possible explanation is that the reaction rate is not uniform and thus creates roughness on the surface.
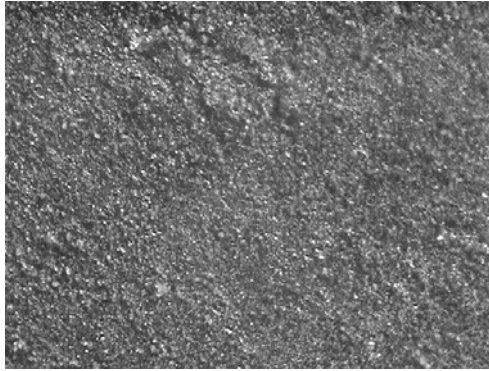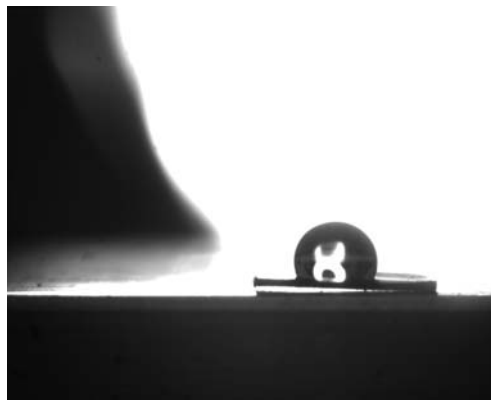

(c) Original gadolinium surface
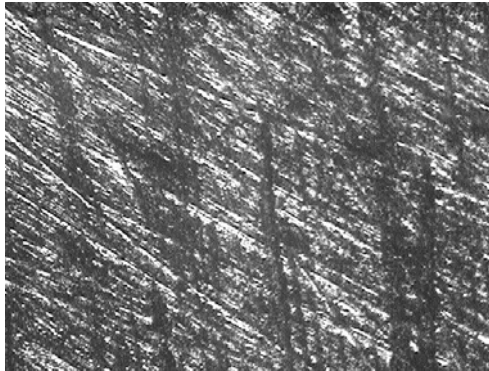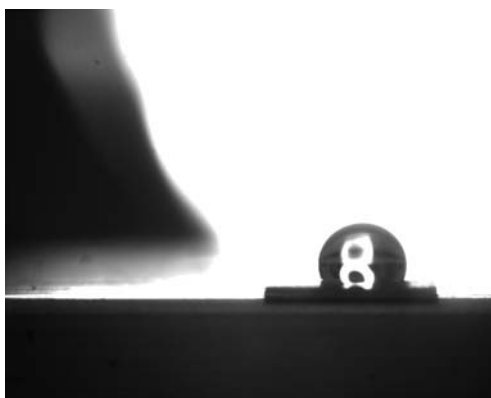

(d) Gadolinium surface after polishing

(e) Gadolinium surface after reaction with HCl

Figure A.1 Images of gadolinium surfaces obtained using an optical microscope (10x): (a) original gadolinium surface; (b) gadolinium surface after polishing; (c) gadolinium surface after reaction with HCl

Figure A.2 shows the contact angles of the three gadolinium surfaces coated with Teflon. The contact angle of the original Teflon-coated gadolinium surface is approximately 110°, the contact angle of the Teflon-coated polished gadolinium surface is also approximately 110°, but the contact angle of the Teflon-coated HCl-treated gadolinium surface is increased to approximately 150° because, according to the Cassie-Baxter model, a rougher surface increases the hydrophobic character of hydrophobic surfaces.

(a) The contact angle of the original Teflon-coated gadolinium surface is

approximately 110°

(b) The contact angle of the Teflon-coated gadolinium surface after polishing is approximately 110°


(c) The contact angle of the Teflon-coated gadolinium surface after reaction with HCl is approximately 150°

Figure A.2 Contact angles of the Teflon-coated gadolinium surfaces: (a) the contact angle of the original gadolinium surface is approximately 110°; (b) the contact angle of the gadolinium surface after polishing is approximately 110°; (c) the contact angle of the gadolinium surface after reaction with HCl is approximately 150°

Although liquid does not adhere to a superhydrophobic surface, there may be several potential problems regarding the application of the Teflon-coated, HCl-treated

gadolinium in the device described here. One problem is that a layer of air is trapped between the liquid and the rough surface, which decreases the thermal contact conductance. Another problem is that gadolinium can also react with hydrogen chloride, as shown in equation A.3 [28]. Therefore, the magnetic force between the gadolinium and the permanent magnet is reduced. In conclusion, more experiments should be performed to determine whether the Teflon-coated, HCl-treated gadolinium is suitable for use in the device described in this work.

$$Gd + 3HCl \rightarrow GdCl_3 + \frac{3}{2} H_2 \qquad (A.3)$$
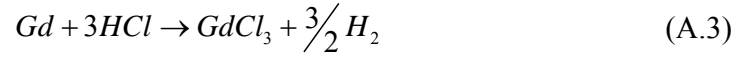
REFERENCES

[1]   H. Eren, "Wireless Sensors and Instruments: Networks, Design, and Applications", *Taylor & Francis, Boca Raton, FL.*, 2006.

[2]   K. Romer, and F. Mattern, "The Design Space of Wireless Sensor Networks", *IEEE Wireless Commun. Mag*, Vol. 11(54), 2004, pp. 54-61.

[3]   Nicholas S. Hudaka, and Glenn G. Amatucc, "Small-scale energy harvesting through thermoelectric, vibration, and radio frequency power conversion", *Journal of Applied Physics*, Vol. 103(10), 2008, pp. 101301.

[4]   C. Shearwood, and R. B. Yates, "Development of an electromagnetic microgenerator", *Electron. Lett.*, Vol. 33, 1997, pp. 1883-1884.

[5]   C. B. Williams, C. Shearwood, M. A. Harradine, P. H. Mellor, T. S. Birch, and R. B. Yates, *Comments. Astrophys.*, 2001, Vol. 148, pp. 337.

[6]   S. R. Anton and H. A. Sodano, "Toward Broadband Vibration-based Energy Harvesting", *Smart Mater. Struct.*, 2007, Vol. 21, pp. 1867-1897.

[7]   S. Priya, *J. Electroceram.*, 2007, Vol. 19, pp. 165.

[8]   S. Roundy, P. K. Wright, and J. Rabaey, "A study of low level vibrations as a power source for wireless sensor nodes", Comput. Commun., 2003, Vol. 26, pp. 1131-1144.

[9]   S. Meninger, J. O. Mur-Miranda, R. Amirtharajah, A. P. Chandrakasan, and J. H. Lang, "Vibration-to-electric energy conversion", *IEEE Transactions on Very Large Scale Integration (VLSI) Systems*, 2001, Vol. 9, pp. 64-76.

[10]   L. Anglesio, A. Benedetto, A. Bonino, D. Colla, F. Martire, S. S. Fusette, and G. d'Amore, Radiat, "Population exposure to electromagnetic fields generated by radio base stations: evaluation of the urban background by using provisional model and instrumental measurements", Radiat Prot Dosimetry., 2001, Vol. 97, pp. 355.

[11]   H. T. Friis, "Friis transmission equation", *Proc. IRE*, 1946, Vol. 34(254).

[12] M. Telkes, "The Efficiency of Thermoelectric Generators", *Journal of Applied Physics*, 1947, Vol. 18, pp. 1116.

[13] J. M. Gordon, "Generalized power versus efficiency characteristics of heat engines: The thermoelectric generator as an instructive illustration", *Am. J. Phys.*, 1991, Vol. 59, pp. 551-555.

[14] Cuadras A, Gasulla M, and Ferrari V., "Thermal energy harvesting through pyroelectricity," *Sensors and Actuators A: Physical*, 2010, Vol. 158, pp.158-132.

[15] M. Ujihara, and G. P. Carman, "Thermal energy harvesting device using ferromagnetic materials", *Applied Physics Letters*, 2007, Vol. 91, pp. 093508.

[16] Katherine Elizabeth Bulgrin, "Magnetic Thermomechanical Devices used for Waste Heat Energy Harvesting and Thermal Conductance Switching", *A dissertation for the degree Doctor of Philosophy in Mechanical Engineering of UCLA*, 2011.

[17] Katherine E. Bulgrin, Y. Sungtaek Ju, Greg P. Carman and Adrienne S. Lavine, "A Coupled Thermal and Mechanical Model of a Thermal Energy Harvesting Device", *IMECE*, 2009-13040, pp. 327-335.

[18] Song, W., Sutton, M. S., and Talghader, J. J., "Thermal contact conductance of actuated interfaces", *Applied Physics Letters*, 2002, Vol. 81, pp. 1216–1218.

[19] Xu, J., and Fisher, T. S., "Enhancement of thermal interface materials with carbon nanotube arrays", *Int. J. Heat Mass Tran.*, 2006, Vol. 49, pp. 1658–1666.

[20] Zaho, Y., Tong, T., Delzeit, L., Kashani, A., Meyyapan, M., and Majumdar, A., "Interfacial energy and strength of multiwalled-carbon-nanotube-based dry adhesive", *J. Vac. Sci. Technol. B*, 2006, Vol. 24, pp. 331:1–331:5.

[21] Cha, G., and Ju, Y. S., "Reversible thermal interfaces based on microscale dielectric liquid layers", *Appl. Phys. Lett.*, 2009, Vol. 94, 211904:1–211904:3.

[22] Yan, J., Cha, G., and Ju, Y. S., "Switchable Thermal Interfaces Based on Discrete Liquid Droplets", *Micromachines*, 2012, Vol. 3, pp. 10-20.

[23] Cha, G., and Ju, Y. S., "Electric field dependence of the Curie temperature of ferroelectricpoly (vinylidenefluoride-trifluoroethylene) co-polymers for pyroelectric energy harvesting", *Smart Mater. Struct.*, 2012, Vol. 21, pp. 022001.

[24] Yan, J., and Ju, Y. S., "A solid-state refrigerator based on the electrocaloric effect", *Appl. Phys. Lett.*, 2012, Vol. 100, pp. 242901.

[25]   Y. Li, et al. "The application of fixed hydrophobic patterns for confinement of aqueous solutions in proteomic microarrays", *Applied Physics Letters*, 2011, Vol. 99, pp. 073703.

[26]   Ui-Chong Yi, et al. "Soft printing of droplets pre-metered by electrowetting", *Sensors and Actuators A*, 2004, Vol. 114, pp. 347–354.

[27]   http://en.wikipedia.org/wiki/Gadolinium

[28]   http://en.wikipedia.org/wiki/Gadolinium(III)_chloride

[29]   David Quere, "Wetting and Roughness", *Annu. Rev. Mater. Res.*, 2008, Vol. 38, pp. 71–99.